coatings

MDPI

Article

Photovoltaic Characteristics of $CH_3NH_3PbI_3$ Perovskite Solar Cells Added with Ethylammonium Bromide and Formamidinium Iodide

Kousuke Nishi, Takeo Oku *, Taku Kishimoto, Naoki Ueoka and Atsushi Suzuki

Department of Materials Science, The University of Shiga Prefecture, 2500 Hassaka, Hikone, Shiga 522-8533, Japan; os21knishi@ec.usp.ac.jp (K.N.); oi21tkishimoto@ec.usp.ac.jp (T.K.); oh21nueoka@ec.usp.ac.jp (N.U.); suzuki@mat.usp.ac.jp (A.S.)

* Correspondence: oku@mat.usp.ac.jp; Tel.: +81-749-28-8368

Received: 1 April 2020; Accepted: 16 April 2020; Published: 20 April 2020

Abstract: Photovoltaic characteristics of solar cell devices in which ethylammonium (EA) and formamidinium (FA) were added to $CH_3NH_3PbI_3$ perovskite photoactive layers were investigated. The thin films for the devices were deposited by an ordinary spin-coating technique in ambient air, and the X-ray diffraction analysis revealed changes of the lattice constants, crystallite sizes and crystal orientations. By adding FA and EA, surface defects of the perovskite layer decreased, and the photoelectric parameters were improved. In addition, the highly (100) crystal orientations and device stabilities were improved by the EA and FA addition.

Keywords: perovskite solar cells; ethlammonium; formamidinium; microstructure

1. Introduction

Organic-inorganic perovskite solar cells provide photoelectric conversion in wide wavelength ranges and exhibit excellent photovoltaic properties [1–6]. Since the film of $CH_3NH_3PbI_3$ ($MAPbI_3$) can be formed by a spin-coating method, there is an advantage that the production process is easy and low cost. In spite of these merits, there is a serious problem that the stability is extremely low. In order to solve this problem, research and development of devices with higher power conversion efficiency and stability using formamidinium (FA) [7–13], guanidinium [14,15] or alkali metal [16–21] doped perovskites for the methylammonium (MA) site have been conducted.

There also exists research and development of devices with ethylammonium (EA) added to perovskites [22–26]. EA has a larger ionic radius (2.74 Å) than that of MA (2.17 Å), and the addition of EA can be expected to improve stability from the viewpoint of calculations [25,27] and tolerance factor [1]. In addition, there is a report that the thermal stability and crystallinity are higher than those of MA, and the addition of EA to the perovskites showed a surface coating with fewer defects and improves the stability of the device [23,28]. However, it should be noted that excessive addition of EA leads to phase separation, a decrease in crystallinity, and precipitation of PbI_2 as an impurity [29,30].

The purpose of this study is to examine the microstructures and photovoltaic characteristics of FA and EA co-added $CH_3NH_3PbI_3$ perovskite solar cells. The stability of a $MAPbI_3$ perovskite structure might be predicted by calculating the tolerance factor (t-factor) [31–35], which is given by $t = \frac{r_{MA}+r_I}{\sqrt{2}(r_{Pb}+r_I)}$, where r is an ionic radius [36]. When the t-factor is in the range of 0.81–1.1, perovskite structures could be formed [35]. If the t-factor is adjusted to 1.0, perovskite structures with cubic symmetry could be realized. The ionic radii of MA^+, FA^+, EA^+, Pb^{2+}, I^-, Br^-, and Cl^- are 2.17, 2.53, 2.74, 1.19, 2.20, 1.96, and 1.81 Å, respectively [35,36]. By adding FA^+ and EA^+ with larger ionic radii than MA^+, t-factor gets closer to 1, and the stability is expected to be improved. In addition, EA addition is expected to

promote the crystal growth and improve the stability of the device [23,28], and there are few reports on simultaneous addition of FA and EA to the perovskite layer. The effects of the simultaneous addition to the perovskite compounds were analyzed by microstructural and photovoltaic characterization.

2. Materials and Methods

A cross-section and deposition process of the present perovskite solar cells is summarized and shown in Figure 1. A fluorine-doped tin oxide (FTO, Nippon Sheet Glass Company, Ltd., Tokyo, Japan) substrate was dipped and washed in an ultrasonic washing machine using acetone twice and methanol once, and cleaned with flowing N_2. The 0.15 and 0.30 M precursor solutions of TiO_2 were prepared from 0.055 and 0.11 mL titanium disopropoxide bis (acetyl acetonate) (Sigma Aldrich, Tokyo, Japan) and 1-btanol (1.0 mL, Nacalai Tesque, Kyoto, Japan). The solutions were cast on the transparent FTO, and spin-coated at 3000 rpm for 30 s and heat-treated at 125 °C for 5 min [37–39]. The processes with 0.30 M precursor solutions were repeated twice. In order to form a dense electron transport TiO_2, the deposited samples were annealed at 550 °C for 30 min. The mesoporous TiO_2 layer was deposited with TiO_2 nanoparticles (P-25, Aerosil, Tokyo, Japan) and polyethylene glycol (Nacalai Tesque, Kyoto, Japan) in ultrapure water. The solution was blended with acethylacetone (20 µL, Fujifilm Wako Pure Chemical Corporation, Osaka, Japan) and triton-X-1001 (10 µL, Sigma Aldrich, Tokyo, Japan) for 30 min, and allowed to stand for 24 h to remove bubbles from the mixed solution. The prepared TiO_2 mixed solution was spin-coated at 5000 rpm for 30 s and annealed at 550 °C for 30 min, and a mesoporous TiO_2 layer was formed.

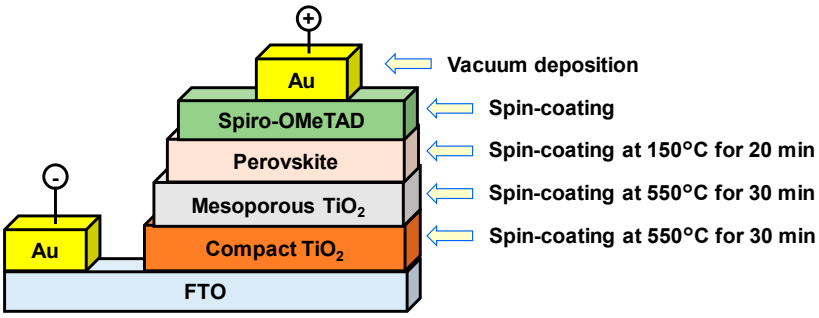

Figure 1. Cross-section of the cell and process conditions.

The perovskite precursor solutions were prepared as mixed solutions of methylamine hydroiodide CH_3NH_3I (MAI, 2.4 M, Tokyo Chemical Industry, Tokyo, Japan) and $PbCl_2$ (0.8 M, Sigma Aldrich, Tokyo, Japan) in *N*,*N*-dimethylformamide (DMF) (0.5 mL, Sigma Aldrich, Tokyo, Japan) at 60 °C for 24 h. This is used as a standard cell, and the amount of MAI was reduced by adding formamidine hydroiodide $CH(NH_2)_2I$ (FAI, Tokyo Chemical Industry, Tokyo, Japan), ethylamine hydrobromide $CH_3CH_2NH_3Br$ (EABr, Tokyo Chemical Industry, Tokyo, Japan), and ethylamine hydrochloride $CH_3CH_2NH_3Cl$ (EACl, Tokyo Chemical Industry, Tokyo, Japan). Detailed compositions of the perovskite compounds are listed in Table 1, together with the *t*-factors. The perovskite precursor solutions were spin-coated at 2000 rpm for 60 s and applied an air-blowing method during spin-coating [40,41]. The device was annealed at 150 °C for 20 min in the ambient air.

The hole-transport layer was deposited by spin-coating. A chlorobenzene solution (0.5 mL) of 2,2′,7,7′-tetrakis-(*N*,*N*-di-p-methoxyphenylamine)-9,9′-spirobifluorene (spiro-OMeTAD, Fujifilm Wako Pure Chemical, Corporation, Osaka, Japan, 36.1 mg) was prepared by mixing it for 12 h. An acetonitrile solution (0.5 mL) of lithium bis (trifluoromethylsulfonyl) imide (Li-TFSI, Tokyo Chemical Industry, Tokyo, Japan) was also prepared by mixing it for 12 h. A mixture solution of the spiro-OMeTAD solution with 4-tertbutylpridine (14.4 µL, Sigma Aldrich, Tokyo, Japan) and Li-TFSI solution (8.8 µL) was prepared by mixing it at 70 °C for 30 min. The spiro-OMeTAD layer was deposited by spin-coating at 4000 rpm for 30 s. After that, gold (Au) thin film electrodes were deposited as electrodes by vacuum

evaporation. As investigated in the previous works [42–44], layer thicknesses of the compact TiO_2, mesoporous TiO_2 + perovskite, spiro-OMeTAD, and Au layers were roughly estimated to be 40, 600, 50, and 200 nm, respectively.

Table 1. Compositions and calculated *t*-factors of the present perovskite compounds.

Composition of Perovskite	EABr (%)	FAI (%)	*t*-Factor
$MAPbI_3$	0	0	0.912
$MA_{0.9}FA_{0.1}PbI_3$	0	10	0.919
$MA_{0.8}FA_{0.2}PbI_3$	0	20	0.927
$MA_{0.5}FA_{0.5}PbI_3$	0	50	0.949
$MA_{0.8}FA_{0.1}EA_{0.1}PbI_{2.7}Br_{0.3}$	10	10	0.933
$MA_{0.75}FA_{0.2}EA_{0.05}PbI_{2.85}Br_{0.15}$	5	20	0.933
$MA_{0.7}FA_{0.2}EA_{0.1}PbI_{2.7}Br_{0.3}$	10	20	0.940
$MA_{0.6}FA_{0.2}EA_{0.2}PbI_{2.4}Br_{0.6}$	20	20	0.954
$MA_{0.75}FA_{0.2}EA_{0.05}PbI_{2.85}Cl_{0.15}$	5	20	0.934
$MA_{0.7}FA_{0.2}EA_{0.1}PbI_{2.7}Cl_{0.3}$	10	20	0.941

The light-induced current density voltage (*J*–*V*) curves of the fabricated devices were obtained by using air mass 1.5 illuminator (San-ei Electric XES-301S, 100 mW·cm^{-2}) and a current-voltage apparatus (B2901A, Keysight, Santa Rosa, CA, USA). In addition, the external quantum efficiencies of the devices were obtained (QE-R, Enli Technology, Kaohsiung, Taiwan). Optical microscopy (Eclipse E600, Nikon, Tokyo, Japan) and X-ray diffraction (D2 PHASER, Bruker, Billerica, MA, USA) measurements were performed to analyze the surface morphologies and nanoscopic structures.

3. Results and Discussion

J–*V* curves collected in the light condition for the fabricated perovskite solar cells are displayed in Figure 2. Table 2 shows summarized parameters of the fabricated solar cells. A conversion efficiency (η) of the standard cell is 6.72%. The J_{SC}, V_{OC} and η were improved from 19.2 mA·cm^{-2}, 0.687 V and 6.72% to 21.5 mA·cm^{-2}, 0.922 V and 14.25% by addition of FA 20% at the MA site. When EA 10% and FA 10% were added simultaneously, the J_{SC}, V_{OC} and η increased 19.9 mA cm^{-2}, 0.946 V and 12.43%. Addition of EACl was also effective for the improvement of the device properties. Further addition of EA and FA would decrease the device performance.

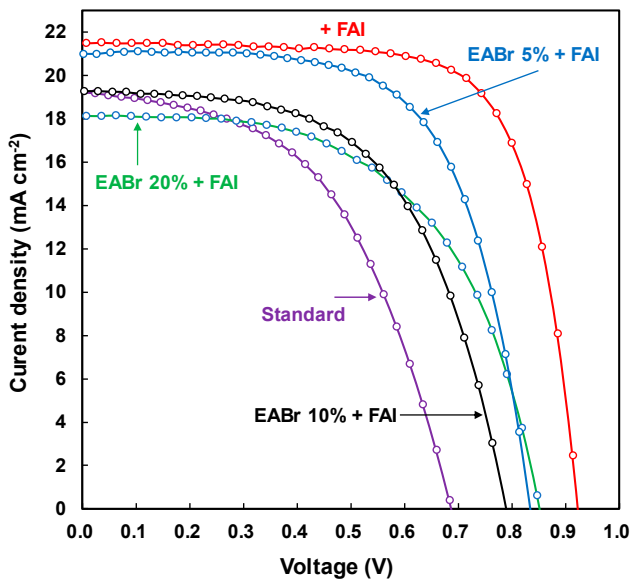

Figure 2. *J*–*V* characteristics collected in light condition for the fabricated solar cells.

Table 2. Measured parameters of the cells fabricated in this study. J_{SC}: short-circuit current density. V_{OC}: open-circuit voltage. FF: fill factor. R_S: series resistance. R_{Sh}: shunt resistance. η: conversion efficiency. η_{ave}: averaged efficiency of three cells.

Device	J_{SC} (mA·cm^{-2})	V_{OC} (V)	*FF*	R_S (Ω·cm^2)	R_{Sh} (Ω·cm^2)	η (%)	η_{ave} (%)
Standard	19.2	0.687	0.509	8.8	337	6.72	6.35
+FAI 10%	21.8	0.816	0.574	6.2	1663	10.24	8.04
+FAI 20%	21.5	0.922	0.719	3.4	4839	14.25	13.66
+FAI 50%	15.7	0.926	0.712	4.7	13,545	10.36	10.31
EABr 10% + FAI 10%	19.9	0.946	0.660	6.1	4667	12.43	12.23
EABr 5% + FAI 20%	21.0	0.834	0.648	5.6	4952	11.33	10.63
EABr 10% + FAI 20%	19.3	0.789	0.572	5.7	1015	8.47	8.70
EABr 20% + FAI 20%	18.1	0.851	0.562	4.8	2340	8.68	8.27
EACl 5% + FAI 20%	20.4	0.879	0.618	6.4	1879	11.06	10.63
EACl 10% + FAI 20%	20.2	0.933	0.647	5.2	66,637	12.21	11.64

Figure 3 is the *J*–*V* curves of the fabricated photovoltaic cells after 4 weeks in ambient air, and the estimated parameters are shown in Table 3. The conversion efficiency of the standard cell was lowered to 5.69%. Co-addition of small amount of EA and FA to $MAPbI_3$ provided higher stability compared with the standard cells, as shown in Figure 4.

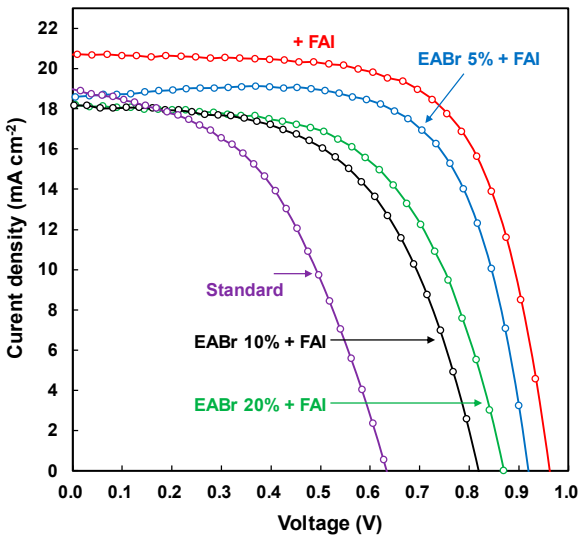

Figure 3. *J*–*V* characteristics collected in light condition for the fabricated solar cells after 4 weeks in ambient air without encapsulation.

Table 3. Measured photovoltaic parameters of the fabricated cells after 4 weeks.

Device	J_{SC} (mA·cm^{-2})	V_{OC} (V)	*FF*	R_S (Ω·cm^2)	R_{Sh} (Ω·cm^2)	η (%)	η_{ave} (%)
Standard	19.0	0.633	0.474	8.9	212	5.69	5.25
+FAI 10%	17.3	0.925	0.615	8.7	5123	9.85	9.30
+FAI 20%	20.7	0.961	0.675	4.6	2455	13.43	13.30
+FAI 50%	14.8	0.964	0.684	6.0	75,968	9.74	8.99
EABr 10% + FAI 10%	17.3	0.925	0.615	8.7	5123	9.85	9.30
EABr 5% + FAI 20%	18.6	0.919	0.699	5.2	19,971	11.93	11.41
EABr 10% + FAI 20%	18.2	0.819	0.564	7.6	1129	8.39	6.86
EABr 20% + FAI 20%	18.2	0.870	0.585	6.6	946	9.26	8.77
EACl 5% + FAI 20%	17.3	0.900	0.682	5.1	4097	10.62	9.98
EACl 10% + FAI 20%	17.0	0.932	0.664	5.8	5407	10.54	9.49

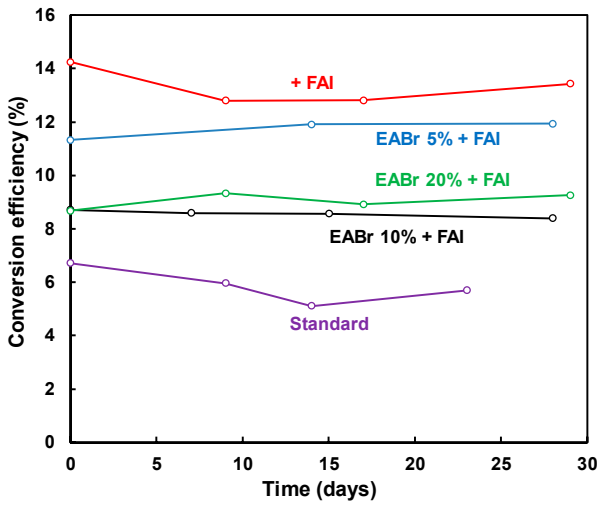

Figure 4. Stability measurements of the fabricated perovskite devices.

Optical microscopy images of the perovskites through spiro-OMeTAD are shown Figure 5. By adding EA and FA, surface defects of the perovskite layer decreased. Obtaining a perovskite layer with few defects enables efficient charge separation and charge extraction, which is thought to have led to improved device performance. In addition, defects in the perovskite layer are a cause of charge recombination, and it is considered that suppression of the defect has led to improvement in stability.

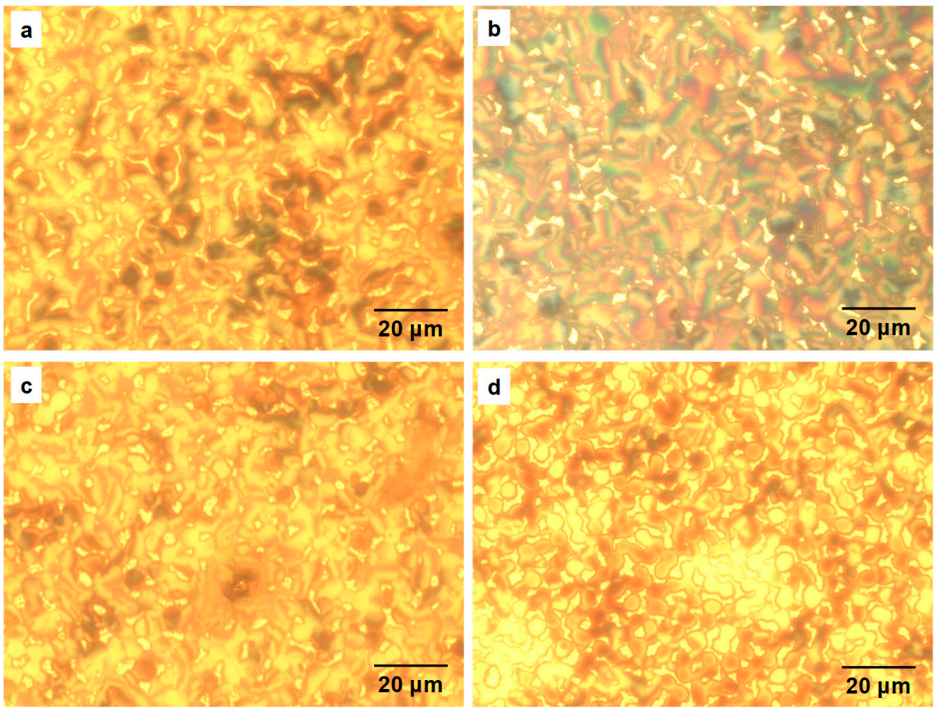

Figure 5. Optical microscopy images of cells with the compositions of (**a**) FAI 20%, (**b**) EABr 5% + FAI 20%, (**c**) EABr 10% + FAI 20%, and (**d**) EABr 20% + FAI 20%.

External quantum efficiency (EQE) spectra of the fabricated photovoltaic cells are shown in Figure 6. The band gap energies (E_g) were estimated from EQE spectra around 800 nm by linear fitting using band gap calculator software (Enli Technology, QE-R), and the measured band gap energies of the perovskite compounds increased from 1.54 to 1.57 eV by adding EA. The E_g value of the 20% EABr-added perovskite crystals was wider than that of the 20%FAI-added perovskite. The EQE values

of the EABr-added device was lower between 350 and 750 nm than that of the FAI-added device, which led to a decrease of the J_{SC} values.

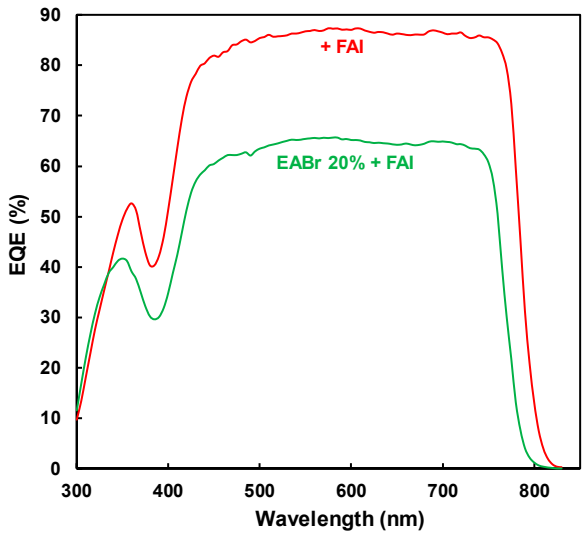

Figure 6. External quantum efficiency spectra of the fabricated solar cells.

X-ray diffraction (XRD) patterns of the fabricated cells added with EABr and FAI are shown in Figure 7a. Increases of (100) and (200) diffraction reflections are observed by adding FAI or EABr. In addition, only (100) and (200) peaks are observed, which indicates that the cells exhibited highly oriented (100) perovskite crystals by the air-blowing method [40].

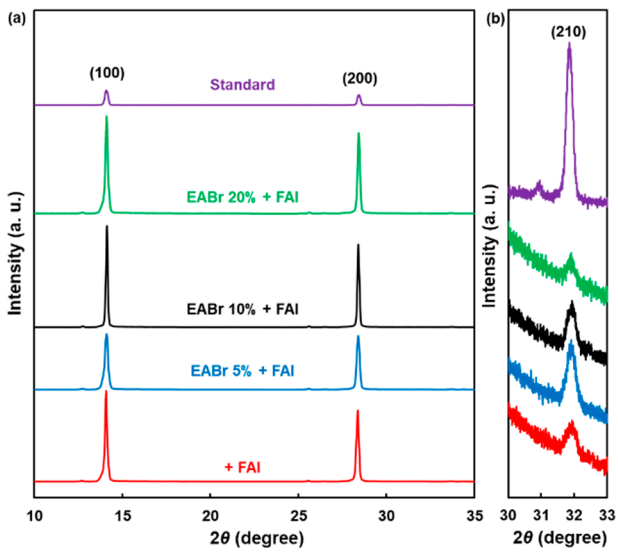

Figure 7. (**a**) X-ray diffraction (XRD) pattern of the present solar cells and (**b**) enlarged pattern of (**a**).

Microstructural parameters of the present perovskite compounds are listed in Table 4. The lattice constants of the FAI-added perovskites were higher compared with the standard $MAPbI_3$ material, whereas those of the EABr and FAI co-added perovskite decreased. Crystallite sizes were estimated from the (200) reflections, and they increased by the addition of FAI and EABr. The I_{100}/I_{210} intensity ratios of (100) reflections (I_{100}) to (210) reflections (I_{210}) were measured from the XRD data in Figure 7a,b, and the results are shown in Table 4. If the $CH_3NH_3PbI_3$ cubic perovskite particles are randomly oriented, then the I_{100}/I_{210} value should be 2.08 [35]. For the standard cell prepared in the present study, the I_{100}/I_{210} is 48, which means the (100) crystal surfaces of the cubic structures are strongly

aligned in the solar cell. By the addition of FAI to the perovskite compounds, I_{100}/I_{210} was increased to 1694, and the I_{100}/I_{210} increased further to 1939 by adding EABr. This is 40 times higher than the I_{100}/I_{210} of the standard perovskite device.

Table 4. Microstructural parameters for the perovskite crystals. Preferred crystal orientations were indicated with ratios of 100 diffraction intensities (I_{100}) to 210 diffraction intensities (I_{210}).

Perovskites	Lattice Constant *a* (Å)	Crystallite Size D_{200} (Å)	Orientation I_{100}/I_{210}
Standard	6.274(1)	479	48
+FAI 20%	6.286(1)	647	1694
EABr 5% + FAI 20%	6.281(0)	528	460
EABr 10% + FAI 20%	6.283(1)	1506	1155
EABr 20% + FAI 20%	6.280(2)	830	1939

A schematic model showing molecular structures (MA, FA, and EA) and the lattice structure of the FAI and EABr added perovskites is shown in Figure 8a,b, respectively. The lattice constant *a* of 6.315 Å for a perovskite single crystal [35,45] is greater compared with the *a* of the perovskite compound in a cell configuration [46,47]. If the perovskite particles were synthesized and deposited on the mesoporous TiO_2 layer, some of the CH_3NH_2 molecules might be desorbed. Then, MA vacancies could be formed, and the lattice constant (6.274 Å) of $MAPbI_3$ is smaller than that of single crystal, as listed in Table 4. When FAI was added to the standard $MAPbI_3$, the FA would occupy the defects and MA sites, and the lattice constant increased to 6.286 Å, as shown in Figure 8b and Table 4. As the size of Br^- is fairly small compare with that of I^-, *a* values of the EABr-added crystals decreased to 6.280 Å compared with FAI-added perovskite crystals, as indicated by arrows in Figure 8b. Combination of the present EA/FA with other molecules [15,48] and alkali metals [21,49] might also be effective for the stabilization of the perovskite compounds.

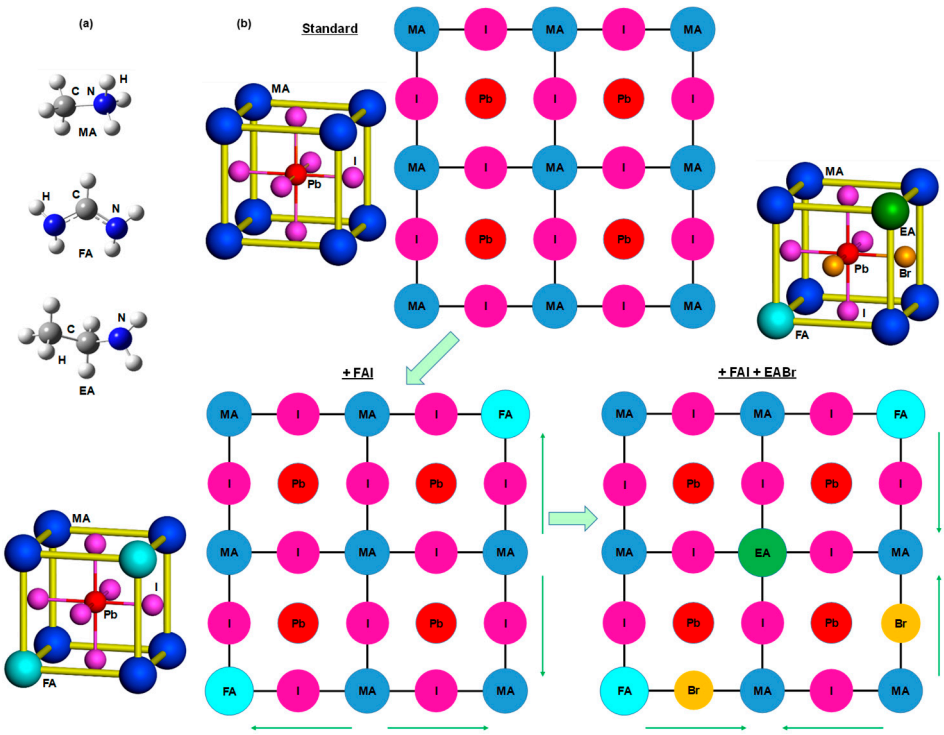

Figure 8. Structures of (**a**) methylammonium (MA), formamidinium (FA), ethylammonium (EA) and (**b**) the present perovskite compounds.

4. Conclusions

Solar cells using perovskite in the photoactive layer were produced by using spin-coating technique in ordinary air, and the influence on photovoltaic characteristics by adding EA and FA to the perovskite phase was investigated. From the results of *J*–*V* characteristics, the addition of EA and FA improved V_{OC} and FF, leading to an improvement in photoelectric conversion efficiency. Devices with EA and FA added maintained photoelectric conversion efficiencies even after 4 weeks compared to that of the standard device. Optical microscope results showed surface improvement, and X-ray diffraction results showed FA and EA substitution at MA position of the perovskite. By substituting FA and EA, which have larger ionic radii than MA, the perovskite structures would have more stable cubic structures with higher stability.

Author Contributions: Conceptualization, K.N. and T.O.; Methodology, K.N., T.K., N.U., and A.S.; Formal Analysis, K.N. and T.O.; Investigation, K.N.; Data Curation, K.N. and T.O.; Writing-Original Draft Preparation, K.N. and T.O.; Writing-Review & Editing, T.O.; Visualization, K.N. and T.O.; Supervision, T.O.; Project Administration, T.O.; Funding Acquisition, T.O. All authors have read and agreed to the published version of the manuscript.

Funding: This research was partly funded by the Super Cluster Program of the Japan Science and Technology Agency (JST).

Conflicts of Interest: The authors declare no conflict of interest.

References

1. Green, M.A.; Ho-Baillie, A.; Snaith, H.J. The emergence of perovskite solar cells. *Nat. Photon* **2014**, *8*, 506–514. [CrossRef]
2. Chen, Q.; Marco, N.D.; Yang, Y.M.; Song, T.B.; Chen, C.C.; Zhao, H.; Hong, Z.; Zhou, H.; Yang, Y. Under the spotlight: The organic—Inorganic hybrid halide perovskite for optoelectronic applications. *Nanotoday* **2015**, *10*, 355–396. [CrossRef]
3. Chen, Y.; He, M.; Peng, J.; Sun, Y.; Liang, Z. Structure and growth control of organic-inorganic halide perovskites for optoelectronics: From polycrystalline films to single crystals. *Adv. Sci.* **2016**, *3*, 1500392. [CrossRef] [PubMed]
4. Saliba, M.; Correa-Baena, J.P.; Wolff, C.M.; Stolterfoht, M.; Phung, N.; Albrecht, S.; Neher, D.; Ababe, A. How to make over 20% efficient perovskite solar cells in regular (n–i–p) and inverted (p–i–n) architectures. *Chem. Mater.* **2018**, *30*, 4193–4201. [CrossRef]
5. Wu, C.; Chen, K.; Guo, D.Y.; Wang, S.L.; Li, P.G. Cations substitution tuning phase stability in hybrid perovskite single crystals by strain relaxation. *RSC Adv.* **2018**, *8*, 2900–2905. [CrossRef]
6. Zhao, Y.; Ye, Q.; Chu, Z.; Gao, F.; Zhang, X.; You, J. Recent progress in high-efficiency planar-structure perovskite solar cells. *Energy Environ. Mater.* **2019**, *2*, 93–106. [CrossRef]
7. Weller, M.T.; Weber, O.J.; Frost, J.M.; Walsh, A. Cubic perovskite structure of black Formamidinium Lead Iodide, α-$[HC(NH_2)_2]PbI_3$, at 298 K. *J. Phys. Chem. Lett.* **2015**, *6*, 3209–3212. [CrossRef]
8. Zhao, Y.; Tan, H.; Yuan, H.; Yang, Z.; Fan, J.Z.; Kim, J.; Voznyy, O.; Gong, X.; Quan, L.N.; Tan, C.S.; et al. Perovskite seeding growth of formamidinium-lead-iodide-based perovskites for efficient and stable solar cells. *Nature* **2018**, *9*, 1607. [CrossRef]
9. Yang, W.S.; Park, B.W.; Jung, E.H.; Jeon, N.J.; Kim, Y.C.; Lee, D.U.; Shin, S.S.; Seo, J.; Kim, E.K.; Noh, J.H.; et al. Iodide management in formamidinium-lead-halide-based perovskite layers for efficient solar cells. *Science* **2017**, *356*, 1376–1379. [CrossRef]
10. Chen, Z.; Zheng, X.; Yao, F.; Ma, J.; Tao, C.; Fang, G. Methylammonium, formamidinium and ethylenediamine mixed triple-cation perovskite solar cells with high efficiency and remarkable stability. *J. Mater. Chem. A* **2018**, *6*, 17625–17632. [CrossRef]
11. Shao, S.; Dong, J.; Duim, H.; Brink, G.H.T.; Black, G.R.; Portale, G.; Loi, M.A. Enhancing the crystallinity and perfecting the orientation of formamidinium tin iodide for highly efficient Sn-based perovskite solar cells. *Nano Energy* **2019**, *60*, 810–816. [CrossRef]
12. Tavakoli, M.M.; Yadav, P.; Prochowicz, D.; Sponseller, M.; Osherov, A.; Bulovic, V.; Kong, J. Controllable perovskite crystallization via antisolvent technique using chloride additives for highly efficient planar perovskite solar cells. *Adv. Energy Mater.* **2019**, *9*, 1803587. [CrossRef]

13. Lu, Y.A.; Chang, T.H.; Wu, S.H.; Liu, C.C.; Lai, K.W.; Chang, Y.C.; Lu, H.C.; Chu, C.W.; Ho, K.C. Coral-like perovskite nanostructures for enhanced light-harvesting and accelerated charge extraction in perovskite solar cells. *Nano Energy* **2019**, *58*, 138–146. [CrossRef]
14. Alharbi, E.A.; Alyamani, A.Y.; Kubicki, D.J.; Uhl, A.R.; Walder, B.J.; Alanazi, A.Q.; Luo, J.; Burgos-Caminal, A.; Albadri, A.; Albrithen, H.; et al. Atomic-level passivation mechanism of ammonium salts enabling highly efficient perovskite solar cells. *Nat. Commun.* **2019**, *10*, 3008. [CrossRef] [PubMed]
15. Kishimoto, T.; Suzuki, A.; Ueoka, N.; Oku, T. Effects of guanidinium addition to $CH_3NH_3PbI_{3-x}Cl_x$ perovskite photovoltaic devices. *J. Ceram. Soc. Jpn.* **2019**, *127*, 491–497. [CrossRef]
16. Hu, Y.; Ayguler, M.F.; Petrus, M.L.; Bein, T.; Docampo, P. Impact of rubidium and cesium cations on the moisture stability of multiple-cation mixed-halide perovskites. *ACS Energy Lett.* **2017**, *2*, 2212–2218. [CrossRef]
17. Hu, Y.; Hutter, E.M.; Rieder, P.; Grill, I.; Hanisch, J.; Ayguler, M.F.; Hufnagel, A.G.; Handloser, M.; Bein, T.; Hartschuh, A.; et al. Understanding the role of cesium and rubidium additives in perovskite solar cells: Trap states, charge transport, and recombination. *Adv. Energy Mater.* **2018**, *8*, 1703057. [CrossRef]
18. Zhao, W.; Yao, Z.; Yu, F.; Yang, D.; Liu, S.F. Alkali metal doping for improved $CH_3NH_3PbI_3$ perovskite solar cells. *Adv. Sci.* **2018**, *5*, 1700131. [CrossRef]
19. Ling, T.; Zou, X.; Cheng, J.; Yang, Y.; Ren, H.; Chen, D. Modulating surface morphology related to crystallization speed of perovskite grain and semiconductor properties of optical absorber layer under controlled doping of potassium ions for solar cells. *Materials* **2018**, *11*, 1605. [CrossRef]
20. Machiba, H.; Oku, T.; Kishimoto, T.; Ueoka, N.; Suzuki, A. Fabrication and evaluation of K-doped $MA_{0.8}FA_{0.1}K_{0.1}PbI_3$(Cl) perovskite solar cells. *Chem. Phys. Lett.* **2019**, *730*, 117–123. [CrossRef]
21. Ueoka, N.; Oku, T.; Suzuki, A. Additive effects of alkali metals on Cu-modified $CH_3NH_3PbI_{3-\delta}Cl_\delta$ photovoltaic devices. *RSC Adv.* **2019**, *9*, 24231–24240. [CrossRef]
22. Hsu, H.L.; Chang, C.C.; Chen, C.P.; Jiang, B.H.; Jeng, R.J.; Cheng, C.H. High-performance and high-durability perovskite photovoltaic devices prepared using ethylammonium iodide as an additive. *J. Mater. Chem. A* **2015**, *3*, 9271–9277. [CrossRef]
23. Zheng, H.; Liu, G.; Chen, X.; Zhang, B.; Alsaedi, A.; Hayat, T.; Pan, X.; Dai, S. High-performance mixed-dimensional perovskite solar cells with enhanced stability against humidity, heat and UV light. *J. Mater. Chem. A* **2018**, *6*, 20233–20241. [CrossRef]
24. Wang, Y.; Zhang, T.; Li, G.; Xu, F.; Li, Y.; Yang, Y.; Zhao, Y. A mixed-cation lead iodide $MA_{1-x}EA_xPbI_3$ absorber for perovskite solar cells. *J. Energy Chem.* **2018**, *27*, 215–218. [CrossRef]
25. Liu, D.; Li, Q.; Wu, K. Ethylammonium as an alternative cation for efficient perovskite solar cells from first-principles calculations. *RSC Adv.* **2019**, *9*, 7356–7361. [CrossRef]
26. Dhar, A.; Dey, A.; Maiti, P.; Paul, P.K.; Roy, S.; Paul, S.; Vekariya, R.L. Fabrication and characterization of next generation nano-structured organo-lead halide-based perovskite solar cell. *Ionics* **2018**, *24*, 1227–1233. [CrossRef]
27. Arkan, F.; Mohammad, I. Computational modeling of the photovoltaic activities in $EABX_3$ (EA = ethylammonium, B = Pb, Sn, Ge, X = Cl, Br, I) perovskite solar cells. *Comput. Mater. Sci.* **2018**, *152*, 324–330. [CrossRef]
28. Zhang, F.; Cong, J.; Li, Y.; Bergstrand, J.; Liu, H.; Cai, B.; Hajian, A.; Yao, Z.; Wang, L.; Hao, Y.; et al. A facile route to grain morphology controllable perovskite thin films towards highly efficient perovskite solar cells. *Nano Energy* **2018**, *53*, 405–414. [CrossRef]
29. Liu, F.; Dong, Q.; Wong, M.K.; Djiurisic, A.B.; Ng, A.; Ren, Z.; Shen, Q.; Surya, C.; Chan, W.K.; Wang, J.; et al. Perovskite solar cells: Is excess PbI_2 beneficial for perovskite solar cell performance? *Adv. Energy Mater.* **2016**, *6*, 1502206. [CrossRef]
30. Ueoka, N.; Oku, T. Stability characterization of PbI_2-added $CH_3NH_3PbI_{3-x}Cl_x$ photovoltaic devices. *ACS Appl. Mater. Interfaces* **2018**, *10*, 44443–44451. [CrossRef]
31. Hoefler, S.F.; Trimmel, G.; Rath, T. Progress on lead-free metal halide perovskites for photovoltaic applications: A review. *Mon. Chem.* **2017**, *148*, 795–826. [CrossRef]
32. Xu, F.; Zhang, T.; Li, G.; Zhao, Y. Mixed cation hybrid lead halide perovskites with enhanced performance and stability. *J. Mater. Chem. A* **2017**, *5*, 11450–11461. [CrossRef]
33. Sampson, M.D.; Park, J.S.; Schaller, R.D.; Chan, M.K.Y.; Martinson, A.B.F. Transition metal-substituted lead halide perovskite absorbers. *J. Mater. Chem. A* **2017**, *5*, 3578–3588. [CrossRef]

34. Tanaka, H.; Oku, T.; Ueoka, N. Structural stabilities of organic–inorganic perovskite crystals. *Jpn. J. Appl. Phys.* **2018**, *57*, 08RE12. [CrossRef]
35. Oku, T. Crystal structures of perovskite halide compounds used for solar cells. *Rev. Adv. Mater. Sci.* **2020**, *59*. in press. [CrossRef]
36. Shannon, R.D. Revised effective ionic radii and systematic studies of interatomic distances in halides and chalcogenides. *Acta Cryst. A* **1976**, *32*, 751–767. [CrossRef]
37. Taguchi, M.; Suzuki, A.; Oku, T.; Fukunishi, S.; Minami, S.; Okita, M. Effects of decaphenylcyclopentasilane addition on photovoltaic properties of perovskite solar cells. *Coatings* **2018**, *8*, 461. [CrossRef]
38. Oku, T.; Nomura, J.; Suzuki, A.; Tanaka, H.; Fukunishi, S.; Minami, S.; Tsukada, S. Fabrication and characterization of $CH_3NH_3PbI_3$ perovskite solar cells added with polysilanes. *Int. J. Photoenergy* **2018**, *1155*, 1–7. [CrossRef]
39. Taguchi, M.; Suzuki, A.; Oku, T.; Ueoka, N.; Minami, S.; Okita, M. Effects of annealing temperature on decaphenylcyclopentasilane-inserted $CH_3NH_3PbI_3$ perovskite solar cells. *Chem. Phys. Lett.* **2019**, *737*, 136822. [CrossRef]
40. Oku, T.; Ohishi, Y.; Ueoka, N. Highly (100)-oriented $CH_3NH_3PbI_3$ (Cl) perovskite solar cells prepared with NH_4Cl using an air blow method. *RSC Adv.* **2018**, *8*, 10389–10395. [CrossRef]
41. Oku, T.; Ohishi, Y. Effects of annealing on $CH_3NH_3PbI_3$ (Cl) perovskite photovoltaic devices. *J. Ceram. Soc. Jpn.* **2018**, *126*, 56–60. [CrossRef]
42. Oku, T.; Ueoka, N.; Suzuki, K.; Suzuki, A.; Yamada, M.; Sakamoto, H.; Minami, S.; Fukunishi, S.; Kohno, K.; Miyauchi, S. Fabrication and characterization of perovskite photovoltaic devices with TiO_2 nanoparticle layers. *AIP Conf. Proc.* **2017**, *1807*, 020014-1–020014-7.
43. Ueoka, N.; Oku, T.; Suzuki, A.; Sakamoto, H.; Yamada, M.; Minami, S.; Miyauchi, S. Fabrication and characterization of CH_3NH_3(Cs)Pb(Sn)I_3(Cl) perovskite solar cells with TiO_2 nanoparticle layers. *Jpn. J. Appl. Phys.* **2018**, *57*, 02CE03-1–02CE03-7. [CrossRef]
44. Ueoka, N.; Oku, T.; Tanaka, H.; Suzuki, A.; Sakamoto, H.; Yamada, M.; Minami, S.; Miyauchi, S.; Tsukada, S. Effects of PbI_2 addition and TiO_2 electron transport layers for perovskite solar cells. *Jpn. J. Appl. Phys.* **2018**, *57*, 08RE05-1–08RE05-7. [CrossRef]
45. Ren, Y.; Oswald, I.W.H.; Wang, X.; McCandless, G.T.; Chan, J.Y. Orientation of organic cations in hybrid inorganic−organic perovskite $CH_3NH_3PbI_3$ from subatomic resolution single crystal neutron diffraction structural studies. *Cryst. Growth Des.* **2016**, *16*, 2945–2951. [CrossRef]
46. Oku, T.; Zushi, M.; Imanishi, Y.; Suzuki, A.; Suzuki, K. Microstructures and photovoltaic properties of perovskite-type $CH_3NH_3PbI_3$ compounds. *Appl. Phys. Express* **2014**, *7*, 121601. [CrossRef]
47. Oku, T.; Ohishi, Y.; Suzuki, A. Effects of antimony addition to perovskite-type $CH_3NH_3PbI_3$ photovoltaic devices. *Chem. Lett.* **2016**, *45*, 134–136. [CrossRef]
48. Jodlowski, A.; Roldán-Carmona, C.; Grancini, G.; Salado, M.; Ralaiarisoa, M.; Ahmad, S.; Koch, N.; Camacho, L.; Miguel, G.; Nazeeruddin, M. Large guanidinium cation mixed with methylammonium in lead iodide perovskites for 19% efficient solar cells. *Nat. Energy* **2017**, *2*, 972–979. [CrossRef]
49. Jalebi, M.A.; Garmaroudi, Z.A.; Pearson, A.J.; Divitini, G.; Cacovich, S.; Philippe, B.; Rensmo, H.; Ducati, C.; Friend, R.H.; Stranks, S.D. Potassium- and rubidium-passivated alloyed perovskite films: Optoelectronic properties and moisture stability. *ACS Energy Lett.* **2018**, *3*, 2671–2678. [CrossRef]